# Changes in black carbon emissions over Europe due to COVID-19 lockdowns

Nikolaos Evangeliou[1,*], Stephen M. Platt[1], Sabine Eckhardt[1], Cathrine Lund Myhre[1], Paolo Laj[2,3,4], Lucas Alados-Arboledas[5,6], John Backman[7], Benjamin T. Brem[8], Markus Fiebig[1], Harald Flentje[9], Angela Marinoni[10], Marco Pandolfi[11], Jesus Yus-Dìez[11], Natalia Prats[12], Jean P. Putaud[13], Karine Sellegri[14], Mar Sorribas[15], Konstantinos Eleftheriadis[16], Stergios Vratolis[16], Alfred Wiedensohler[17], Andreas Stohl[18]

[1]Norwegian Institute for Air Research (NILU), Department of Atmospheric and Climate Research (ATMOS), Kjeller, Norway.
[2]University of Grenoble Alpes, CNRS, IRD, Grenoble-INP, IGE, 38000 Grenoble, France.
[3]CNR-ISAC, National Research Council of Italy – Institute of Atmospheric Sciences and Climate, Bologna, Italy.
[4]University of Helsinki, Atmospheric Science division, Helsinki, Finland.
[5]Andalusian Institute for Earth System Research (IISTA-CEAMA), Granada, Spain.
[6]Department of Applied Physics, University of Granada, Granada, Spain.
[7]Atmospheric Composition Research, Finnish Meteorological Institute, Helsinki, Finland.
[8]Laboratory of Atmospheric Chemistry, Paul Scherrer Institute, Villigen PSI, Switzerland.
[9]Deutscher Wetterdienst, Meteorologisches Observatorium Hohenpeissenberg, Albin-Schwaiger-Weg 10, 82383 Hohenpeissenberg, Germany.
[10]Institute of Atmospheric Sciences and Climate, National Research Council of Italy (ISAC-CNR), 40121, Bologna, Italy.
[11]Institute of Environmental Assessment and Water Research IDAEA-CSIC, C/Jordi Girona 18-26, Barcelona 08034, Spain.
[12]Izaña Atmospheric Research Center, State Meteorological Agency (AEMET), C/La Marina 20, 38001, Tenerife, Spain.
[13]European Commission, Joint Research Centre (JRC), Via Enrico Fermi 2749, Ispra (VA) 21027, Italy.
[14]Laboratoire de Météorologie Physique, UMR6016, CNRS/UBP, 63178 Aubière, France.
[15]El Arenosillo Atmospheric Sounding Station, Atmospheric Research and Instrumentation Branch, National Institute for Aerospace Technology, 21130 Huelva, Spain.

33   [16]Environmental Radioactivity Lab, Institute of Nuclear & Radiological Sciences &

34   Technology, Energy & Safety, NCSR "Demokritos", Ag. Paraskevi, Athens, Greece.

35   [17]Department Experimental Aerosol and Cloud Microphysics, Leibniz Institute for

36   Tropospheric Research, Leipzig, Germany.

37   [18]Department of Meteorology and Geophysics, University of Vienna, UZA II,

38   Althanstraße 14, 1090 Vienna, Austria.

39

40   **\*** Corresponding author: N. Evangeliou (Nikolaos.Evangeliou@nilu.no)

41

42

## Abstract

Following the emergence of the severe acute respiratory syndrome coronavirus 2 (SARS-CoV-2) responsible for COVID-19 in December 2019 in Wuhan (China) and its spread to the rest of the world, the World Health Organization declared a global pandemic in March 2020. Without effective treatment in the initial pandemic phase, social distancing and mandatory quarantines were introduced as the only available preventative measure. In contrast to the detrimental societal impacts, air quality improved in all countries that strict lockdowns were applied, due to lower pollutant emissions. Here we investigate the effects of the COVID-19 lockdowns in Europe on ambient black carbon (BC), which affects climate and damages health, using in-situ observations from 17 European stations in a Bayesian inversion framework. BC emissions declined by 23 kt in Europe (20% in Italy, 40% in Germany, 34% in Spain, 22% in France) during lockdowns compared to the same period in the previous five years, which is partially attributed to COVID-19 measures. BC temporal variation in the countries enduring the most drastic restrictions showed the most distinct lockdown impacts. Increased particle light absorption in the beginning of the lockdown, confirmed by assimilated satellite and remote sensing data, suggests residential combustion was the dominant BC source. Accordingly, in Central and Eastern Europe, which experienced lower than average temperatures, BC was elevated compared to the previous five years. Nevertheless, an average decrease of 11% was seen for the whole of Europe compared to the start of the lockdown period, with the highest peaks in France (42%), Germany (21%), UK (13%), Spain (11%) and Italy (8%). Such a decrease was not seen in the previous years, which also confirms an impact of COVID-19 on the European emissions of BC.

# 1 Introduction

The identification of the severe acute respiratory syndrome coronavirus 2 (SARS-CoV-2 or COVID-19) in December 2019 (WHO, 2020) in Wuhan (China) and its subsequent transmission to South Korea, Japan, and Europe (initially mainly Italy, France and Spain) and the rest of the world led the World Health Organization to declare a global pandemic by March 2020 (Sohrabi et al., 2020). Although the symptoms are normally mild or not even detected for most of the population, people with underlying diseases or elderly are very vulnerable showing complications that can lead to death (Huang et al., 2020). Considering the lack of available treatment and vaccination to combat further spread of the virus, the only prevention measures included strict social, travel and working restrictions in a so-called lockdown period that lasted for several weeks (mid-March to end of April 2020 for most of Europe). The most drastic measures were taken in China, where the outbreak started, in Italy that faced large human losses and later in the United States. Despite all these restriction, still six months after the first lockdown, several countries are reporting severe human losses due to the virus (John Hopkins University of Medicine, 2020).

Despite the dramatic health and socioeconomic consequences of COVID-19 lockdowns, their environmental impact might be beneficial. Bans on mass gatherings, mandatory school closures, and home confinement (He et al., 2020; Le Quéré et al., 2020) during lockdowns have all resulted in lower traffic-related pollutant emissions and improved air quality in Asia, Europe and America (Adams, 2020; Bauwens et al., 2020; Berman and Ebisu, 2020; Conticini et al., 2020; Dantas et al., 2020; Dutheil et al., 2020; He et al., 2020; Kerimray et al., 2020; Le et al., 2020; Lian et al., 2020; Otmani et al., 2020; Sicard et al., 2020; Zheng et al., 2020). The restrictions also present an opportunity to evaluate the cascading responses from the interaction of humans, ecosystems, and climate with the global economy (Diffenbaugh et al., 2020).

Strongly light absorbing black carbon (BC, or 'soot'), is produced from incomplete combustion of carbonaceous fuels e.g. fossil fuels, wood burning, biofuels (Bond et al., 2013). By absorbing solar radiation, it warms the air, reduces tropical cloudiness (Ackerman, 2000) and atmospheric visibility (Jinhuan and Liquan, 2000). BC causes pulmonary diseases (Wang et al., 2014a), may act as cloud condensation nuclei affecting cloud formation and precipitation (Wang et al., 2016) and contributes to global warming (Bond et al., 2013; Myhre et al., 2013; Wang et al., 2014a). When deposited on snow, it reduces snow albedo (Clarke and Noone, 1985; Hegg et al., 2009) accelerating melting. Since BC is both climate relevant and strongly

99  linked to anthropogenic activity, it is important to determine the effects of the COVID-19

100 lockdowns thereon.

101     Here, we present a rigorous assessment of temporal and spatial changes BC emissions

102 over Europe (including Middle East and parts of North Africa), combining in situ observations

103 from the Aerosol, Clouds and Trace Gases Research Infrastructure (ACTRIS) network and

104 state-of-the-art emission inventories within a Bayesian inversion. We validate our results with

105 independent satellite data and compare them to inventories and baseline and optimized

106 emissions calculated for previous years.

## 2  Methods

108     This section gives a detailed description of all datasets and methods used for the

109 calculation of COVID-19 impact. Section 2.1 describes the instrumentation of the particle light

110 absorption measurements from Aerosol, Clouds and Trace Gases Research Infrastructure

111 (ACTRIS), and the networks European Monitoring and Evaluation Program (EMEP) and

112 Global Atmosphere Watch (GAW). These measurements were used in the inverse modelling

113 algorithm (dependent measurements) and to validate the optimised (posterior) emissions of BC

114 (independent measurements). For each of the observations and stations, the source – receptor

115 matrices (SRMs), also known as "footprint emission sensitivities" or "footprints", were

116 calculated as described in section 2.2. The latter together with the observations were fed in the

117 inversion algorithm described in section 2.3. To overcome classic inverse problems (Tarantola,

118 2005), prior (a priori) emissions of BC were used in the inverse modelling algorithm calculated

119 using bottom-up approaches (section 2.4). The optimised (a posteriori) emissions of BC were

120 compared with reanalysis data from MERRA-2 (Modern-Era Retrospective Analysis for

121 Research and Applications Version 2), which are described in section 2.5, while MERRA-2

122 Ångström exponent data together with absorption Ångström exponent from the aerosol robotic

123 network (AERONET) (section 2.6) were used to examine the presence of biomass burning

124 aerosols in Europe. A description of the statistical tests and the country definitions used in the

125 paper is given in sections 2.7 and 2.8, respectively.

### 2.1  Particle light absorption measurements

127     The measurement sites contributing data to this paper are regional background sites

128 (except for one site in Germany) and all contribute to the research infrastructure ACTRIS, and

129 the networks EMEP and GAW. The measurement data used for the period 2015 - May 2020

130 consist of hourly-averaged, quality-checked, particle light absorption measurements.  The

quality assurance and quality control correspond to the Level 2 requirements for ACTRIS, EMEP and GAW data, as described in detail in Laj et al. (2020).

All absorption measurements within ACTRIS and EMEP are taken using a variety of filter-based photometers: Multi-Angle Absorption Photometers (MAAP), Particle Soot Absorption Photometers (PSAP) Continuous Light Absorption Photometers (CLAP), and the Aethalometer (AE31). Information on instrument type at the various sites are included in Table 1 and procedures for harmonization of measurement protocols to produce comparable data seta are described in Laj et al. (2020) in detail. Zanatta et al. (2016) suggested that a mass absorption cross-section (MAC) value of 10 m$^2$ g$^{-1}$ (geometric standard deviation of 1.33) at a wavelength of 637 nm can be considered to be representative of the mixed boundary layer at European ACTRIS background sites, where BC is expected to be internally mixed to a large extent. Assuming an absorption Ångström exponent (AAE) is equal to unity, i.e. assuming no change in MAC for different sources (Zotter et al., 2017), we extrapolated the MACs at 637 nm ($MAC_{@\lambda 1}$) to the measurement wavelengths of our study ($MAC_{@\lambda 2}$) using the following equation:

$$MAC_{@\lambda 2} = MAC_{@\lambda 1}(\frac{\lambda 1}{\lambda 2})^{AAE} \xrightarrow{yields} MAC_{@\lambda 2} = 10(\frac{637}{\lambda 2})^1 \qquad (1)$$

following Lack and Langridge (2013). The resulting MAC values for each measurement station are shown in Table 1.

## 2.2 Source – receptor matrix (SRM) calculations

SRMs for each of the 17 receptor sites (Table 1) were calculated using the Lagrangian particle dispersion model FLEXPART version 10.4 (Pisso et al., 2019). The model releases computational particles that are tracked backward in time based on 3-hourly operational meteorological analyses from the European Centre for Medium-Range Weather Forecasts (ECMWF) with 137 vertical layers and a horizontal resolution of 1°×1°. The tracking of BC particles includes gravitational settling for spherical particles with an aerosol mean diameter of 0.25 μm and a logarithmic standard deviation of 0.3 and a particle density of 1500 kg m$^{-3}$ (Long et al., 2013). FLEXPART also simulates dry and wet deposition (Grythe et al., 2017), turbulence (Cassiani et al., 2014), unresolved mesoscale motions (Stohl et al., 2005) and includes a deep convection scheme (Forster et al., 2007). SRMs were calculated for 30 days backward in time, at temporal intervals that matched measurements at each receptor site. This backward tracking is sufficiently long to include almost all BC sources that contribute to surface

162 concentrations at the receptors given a typical atmospheric lifetime of 3–11 days (Bond et al.,
163 2013).

## 2.3 **Bayesian inverse modelling**

165     The Bayesian inversion framework FLEXINVERT+ described in detail in Thompson
166 and Stohl (2014) was used to optimize emissions of BC before (January to mid-March 2020)
167 and during the COVID-19 lockdown period in Europe (mid-March to end of April 2020). To
168 show potential differences on the signal from the 2020 restrictions, emissions were optimised
169 with the same set up during the same period (January to April) in the previous five years (2015–
170 2019). Note that the number of stations in the inversions of 2015–2019 was slightly higher (20
171 stations against 15 that were used in 2020), due to different data availability. The algorithm
172 finds the optimal emissions, which lead to FLEXPART modelled concentrations that better
173 match the observations considering the uncertainties for observations, prior emissions and
174 SRMs. Specifically, the state vector of BC concentrations, $y^{mod}_{(M \times 1)}$, at $M$ points in space and
175 time can be modelled given an estimate of the emissions, $x_{(N \times 1)}$, of the $N$ state variables
176 discretised in space and time, while atmospheric transport and deposition are linear operations
177 described by the Jacobian matrix of SRMs, $\mathbf{H}_{(M \times N)}$:

$$y^{mod} = \mathrm{H}x + \epsilon \qquad (2)$$

179 where $\epsilon$ is an error associated with model representation, such as the modelled transport and
180 deposition or the measurements. Since H is not invertible or may not have unique inverse,
181 according to Bayesian statistics, the inverse problem can be described as the maximization of
182 the probability density function of the emissions given the prior information and observations.
183 This is equivalent to the minimun of the cost function:

$$\mathbf{J}(x) = \frac{1}{2}(x - x_b)^T \mathbf{B}^{-1}(x - x_b) + \frac{1}{2}(y - \mathbf{H}x)^T \mathbf{R}^{-1}(y - \mathbf{H}x) \qquad (3)$$

185 where $y$ is the vector of observed BC concentrations, $x$ and $x_b$ the vectors of optimized and
186 prior emissions, respectively, while **B** and **R** are the error covariance matrices that weight the
187 posterior–prior flux and observation–model mismatches, respectively. Based on the Bayes'
188 theorem, the most probable posterior emissions, $x$ are given by the following equation
189 (Tarantola, 2005):

$$x = x_b + \mathbf{B}\mathbf{H}^{\mathbf{T}}(\mathbf{H}\mathbf{B}\mathbf{H}^{\mathbf{T}} + \mathbf{R})^{-1}(y - \mathbf{H}x_b) \qquad (4)$$

191     Here, posterior emissions were calculated weekly between 1 January and 30 April 2020.
192 The aggregated inversion grid (25°N–75°N and 10°W–50°E) and the average SRM for
193 inversions are shown in Figure 1, while the measurement stations are listed in Table 1. The

194 variable grid uses high resolution at regions, where there are many stations and hence strong
195 contribution from emissions, while it lowers resolution at regions that lack measurement
196 stations following a method proposed by Stohl et al. (2010).

197 Prior emission errors **B** are correlated in space and time, but very little is known about
198 the true temporal and spatial error correlation patterns. The spatial error correlation for the
199 emissions is defined as an exponential decay over distance (we assume that emissions on land
200 and ocean are not correlated). The temporal error correlation matrix is described similarly using
201 the time difference between grid cells in different time steps. The full temporal and spatial
202 correlation matrix is given by the Kronecker product (see Thompson and Stohl, 2014). The
203 error covariance matrix for the emissions is the matrix product of correlation pattern and the
204 error covariance of the prior fluxes. We calculate the error on the emissions in each grid-cell
205 (on the fine grid) as a fraction of the maximum value out of that grid cell and the eight
206 surrounding ones.

207 The observation error covariance matrix **R** combines measurement, transport model and
208 representation errors. For the measurement errors, we use values given by the data providers.
209 Transport model errors are difficult to quantify and depend not only on the model but also on
210 the meteorological inputs. Therefore, we do not quantify the full transport error, but only the
211 part of it that can be estimated from FLEXPART, i.e. the stochastic uncertainty (see Stohl et
212 al., 2005). As regards to representation errors, we consider observation representation error and
213 model aggregation error. The observation representation error is calculated from the standard
214 deviation of all measurements available in a user-specified measurement averaging time
215 interval, based on the idea that if the measurements are fluctuating strongly within that interval
216 then their mean value is associated with higher uncertainty than if the measurements are steady
217 (Bergamaschi et al., 2010). The aggregation error is attributed to reduction of the spatial
218 resolution of the model and is calculated by projecting the loss of information in the state space
219 into the observation space (Kaminski et al., 2001). Hence, the observation error covariance
220 matrix is defined as the diagonal matrix with elements equal to the quadratic sum of the
221 measurement, transport model and measurement representation errors (Thompson and Stohl,
222 2014).

223 Theoretically, the algorithm can calculate negative posterior emissions, which are
224 physically unlikely. To tackle this problem, an inequality constraint was applied on the
225 emissions following the method of Thacker (2007) that applies the constraint as "error-free"
226 observations:

227 $$\hat{x} = x + \mathbf{A}\mathbf{P}^{\mathbf{T}}(\mathbf{P}\mathbf{A}\mathbf{P}^{\mathbf{T}})^{-1}(c - \mathbf{P}x) \qquad (5)$$

where **A** is the posterior error covariance matrix, **P** is a matrix operator to select the variables that violate the inequality constraint, and $c$ is a vector of the inequality constraint, which in this case is zero.

We evaluated the assumptions made on the error covariance matrices for the prior emissions and the observations using the reduced $\chi^2$ statistics (**B** and **R**). When $\chi^2$ is equal to unity, the posterior solution is within the limits of the prescribed uncertainties. The latter is the value of the cost function at the optimum (Thompson et al., 2015). In the inversions performed here, the calculated $\chi^2$ values were between 0.8 and 1.5 indicating that the chosen uncertainty parameters are close to the ideal ones. The number of measurements used in each inversion was equal to 12538 from 17 stations. To select the inversion that provides the most statistically significant result, an evaluation of the improvement in the posterior modelled concentrations, with respect to the prior ones, against the observations was performed (Figure 2). The resulting values of each of the statistical measures that were performed are given in detail in Table 2. Note that this is not a validation of the posterior emissions, because the comparison is only done for the observations that were included in the inversion (dependent observations), and the inversion algorithm has been designed to reduce the model–observation mismatches. This means that the reduction of the posterior concentration mismatches to the observations is determined by the weighting that is given to the observations with respect to the prior emissions. A proper validation of the posterior emissions is performed against observations that were not included in the inversion (independent observations) in section 3.3.

**2.4   Prior emissions**

As a priori emissions in the inversions, the ECLIPSE version 5 and 6 (Evaluating the CLimate and Air Quality ImPacts of ShortlivEd Pollutants) (Klimont et al., 2017), EDGAR (Emissions Database for Global Atmospheric Research) version HTAP_v2.2 (Janssens-Maenhout et al., 2015), ACCMIP (Emissions for Atmospheric Chemistry and Climate Model Intercomparison Project) version 5 (Lamarque et al., 2013) and PKU (Peking University) (Wang et al., 2014b) were used (Figure 3). All inventories include the basic emission sectors (e.g., waste burning, industrial combustion and processing, all means of transportation (aerial, surface, ocean), energy conversion, residential and commercial combustion (see references therein). Biomass burning emissions were adopted from the Global Fire Emissions Database, Version 4.1s (GFEDv4.1s)(Giglio et al., 2013). Note that the a priori emissions used in the inversions of 2015–2019 period corresponded to year 2015 of ECLIPSEv6 and they were not interpolated for the years between 2015 and 2020, where the ECLIPSEv6 emissions were

calculated for. We calculate that the anthropogenic emissions of BC in Europe between January-April 2015 and January-April 2020 in ECLIPSEv6 differ by 3.4% only, and therefore we expect that this would not add significant bias in our calculations.

## 2.5 MERRA-2 (Modern-Era Retrospective Analysis for Research and Applications Version 2)

The MERRA-2 reanalysis dataset for BC (Randles et al., 2017) assimilates bias-corrected AOD from Moderate Resolution Imaging Spectroradiometer (MODIS), Advanced Very High Resolution Radiometer (AVHRR) instruments, Multiangle Imaging SpectroRadiometer (MISR) and Aerosol Robotic Network (AERONET) with the Goddard Earth Observing System Model Version 5 (GEOS-5). BC and other aerosols in MERRA-2 are simulated with the Goddard Chemistry, Aerosol, Radiation and Transport (GOCART) model and delivered in hourly to monthly temporal resolution and $0.5° \times 0.625°$ spatial. The product has been validated for AOD, PM and BC extensively (Buchard et al., 2017; Qin et al., 2019; Randles et al., 2017; Sun et al., 2019). Ångström exponent (AE), a measure of how the AOD changes relative to the various wavelength of light, is derived here from AOD469, AOD550, AOD670, and AOD865, by fitting the data to the linear transform of Ångström's empirical expression:

$$\tau_\lambda = \tau_{\lambda_0} \left(\frac{\lambda}{\lambda_0}\right)^{-a} \qquad (6)$$

where $\tau_\lambda$ is the known AOD at wavelength $\lambda$ (in nm), $\tau_{\lambda_0}$ is the AOD at 1000 nm, and α stands for AE (Gueymard and Yang, 2020).

## 2.6 Absorption Ångström exponent from Aerosol Robotic Network (AERONET) data

Aerosol composition over Europe during the COVID-19 lockdown was confirmed using the AERONET data (Holben et al., 1998). AERONET provides globally distributed observations of spectral aerosol optical depth (AOD), inversion products, and precipitable water in diverse aerosol regimes. The AE for a spectral dependence of 440-870 nm is related to the aerosol particle size. Values less than 1 suggest an optical dominance of coarse particles corresponding to dust, ash and sea spray aerosols, while values greater than one imply dominance of fine particles such as smoke and industrial pollution (Eck et al., 1999). We chose data from five stations covering Western, Central and Eastern Europe, for which cloud-free measurements exist for the lockdown period, namely Ben Salem (9.91°E, 35.55°N), Minsk (27.60°E, 53.92°N), Montsec (0.73°E, 42.05°N), MetObs Lindenberg (14.12°E, 52.21°N) and

292 Munich University (11.57°E, 48.15°N). We used Level 1.5 absorption AE (AAE)
293 measurements for the COVID-19 lockdown period (14 March to 30 April 2020).

**2.7  Statistical measures**

295     For the performance evaluation of the inversion results against dependent (observations
296 that were included in the inversion) and independent observations (observations that were not
297 included in the inversion), four different statistical quantities were used:

298 (1) Pearson's correlation coefficient:

$$R_{mo} = \frac{n\sum_{i=1}^{n} m_i o_i - \sum_{i=1}^{n} m_i \sum_{i=1}^{n} o_i}{\sqrt{n\sum_{i=1}^{n} m_i^2 - (\sum_{i=1}^{n} m_i)^2}\sqrt{n\sum_{i=1}^{n} o_i^2 - (\sum_{i=1}^{n} o_i)^2}} \qquad (7)$$

300 where $n$ is sample size, $m$ and $o$ the individual sample points for model concentrations and
301 observations indexed with $i$.

302 (2) The normalized root mean square error (nRMSE):

$$nRMSE = \frac{\sqrt{\sum_{i=1}^{n} \frac{1}{n}(m_i - o_i)^2}}{o_i^{max} - o_i^{min}} \qquad (8)$$

304 (3) The mean fractional bias $MFB$ was selected as a symmetric performance indicator that gives
305 equal weights to under- or over-estimated concentrations (minimum to maximum values range
306 from -200% to 200%) and is defined as:

$$MFB = \frac{1}{n} \frac{\sum_{i=1}^{n}(m_i - o_i)}{\sum_{i=1}^{n}(\frac{m_i + o_i}{2})} \qquad (9)$$

308 (4) The mean absolute error was computed normalized ($nMAE$) over the average of all the
309 actual values (observations here), which is a widely used simple measure of error:

$$nMAE = \frac{\sum_{i=1}^{n}|m_i - o_i|}{\sum_{i=1}^{n} o_i} \qquad (10)$$

**2.8  Region definitions**

312     All country and regional masks are publicly available. Regions used for statistical
313 processing purposes were adopted from the United Nations Statistics Division
314 (https://unstats.un.org/home/). Accordingly, Northern Europe includes UK, Norway, Denmark,
315 Sweden, Finland, Iceland, Estonia, Latvia and Lithuania. Southern Europe includes Spain, Italy,
316 Greece, Slovenia, Croatia, Bosnia, Serbia, Albania and North Macedonia. Western Europe is
317 defined by France, Belgium, Holland, Germany, Austria and Switzerland. Eastern Europe
318 includes Poland, Czechia, Slovakia, Hungary, Romania, Bulgaria, Moldova, Ukraine, Belarus
319 and Russia.

# 3 Results

## 3.1 Optimized (posterior) emissions from Bayesian inversion

We performed five inversions for BC over Europe for 1st January- 30th April 2020, each with different prior emissions from ECLIPSE version 5 and 6, EDGAR version HTAP_v2.2, ACCMIP version 5 and PKU (Figure 3). Total prior emissions of BC in Europe from the five emission inventories for the period of the inversion ranged between 192-377 kt. We evaluated the assumptions made on the error covariance matrices for the prior emissions and the observations using the reduced $\chi^2$ statistic (**B** and **R**, see section 2.3). When $\chi^2$ is equal to unity, the posterior solution is within the limits of the prescribed uncertainties. The performance of the inversions with the five different prior inventories was evaluated using four statistical parameters (see section 2.7). The best performance of the inversions was achieved using ECLIPSEv6 (Table 2 and Figure 2) with the smallest $nRMSE$ (0.073) value, the largest Pearson's $R^2$ (0.60), the closest to zero $MFB$ value (0.03) and the smallest $nMAE$ (714). Therefore, all the results presented below correspond to this inversion.

Posterior emissions of BC were calculated to be 191 kt in the inversion domain (10°W–50°E, 25°N–75°N) or approximately 20% smaller than those in ECLIPSEv6 (239 kt) (Figure 4). Note that these numbers refer to the whole inversion domain (not only Europe) and the whole study period (January – April 2020). The largest posterior differences were found in the eastern part of the domain (20°E–50°E, 45°N–55°N), where emissions dropped from 35 to 29 kt. Emissions of BC in the western part of the inversion domain (10°W–20°E, 45°N–55°N) declined by almost 11% (from 45 to 40 kt), as those in the north part (5°W–35°E, 55°N–70°N) that covers Scandinavian countries (from 8.7 to 6.4 kt). Finally, in the southern part (10°W–50°E, 35°N–45°N) of the domain (Spain, Italy, Greece) the posterior emissions also decreased by 21% relative to the priors (from 61 to 48 kt). The largest country decreases were seen in France (from 14 to 8.2 kt), Italy (from 8.0 to 5.9 kt), UK (from 4.4 to 3.1 kt) and Germany (from 4.5 to 4.1 kt). Surprisingly, BC emissions were slightly enhanced in Poland (from 21 to 23 kt), and in Spain (from 6.3 to 7.5 kt). In general, inversion algorithms reduce the mismatches between modelled concentrations and observation by correcting emissions (section 2.3). If decreased posterior emissions are calculated during the whole inversion period (before and during the lockdowns), impact from the COVID-19 restrictions cannot be concluded and, most likely, the reduced emissions are due to errors in the prior emissions. In the next section (3.2), we demonstrate that this decrease was due to the COVID-19 lockdowns, by comparing

352 posterior emissions with emissions from previous years, as well as with the respective

353 emissions before and during the lockdown measures.

354 **3.2 Comparison with previous years**

355       We also performed inversions for 2015–2019 for the same period as the 2020 lockdowns

356 (January- April) using almost the same measurement stations and keeping the same settings.

357 The difference in BC emissions during the lockdown in 2020 (14 March to 30 April) from the

358 respective emissions during the same period in 2015–2019 (14 March to 30 April) are shown

359 in Figure 5 (a, emission anomaly) together with the gross domestic product (GDP) (Kummu et

360 al., 2020) (b) , and (c) temperature anomaly from ERA-5 (Copernicus Climate Change Service

361 (C3S), 2020) for the same period as the emission anomaly. The difference in the 2020 emissions

362 of BC during the lockdown from the respective emissions in the same period in each of the

363 previous years (2015–2019) is illustrated in Supplementary Figure 1. As an independent source

364 of information, active fires from MODIS satellite product MCD14DL (Giglio et al., 2003) are

365 also shown in Figure 5a and Supplementary Figure 1.

366       Overall, BC emissions decreased by ~46 kt during the COVID-19 lockdown in the

367 inversion domain (10°W–50°E, 25°N–70°N) as compared with the same period in the previous

368 five years. We record a significant decrease in BC emissions in Central Europe (Northern Italy,

369 Austria, Germany, Spain and some Balkan countries) (Figure 5). On average, emissions were

370 23 kt lower (63 to 40 kt) over Europe during the lockdown in 2020 than in the same period of

371 2015–2019 (Figure 5). The decrease has the same characteristics when compared to each of

372 previous years since 2015 (Supplementary Figure 1) based on measurements of BC at similar

373 regions as those used for the 2020 inversion. The countries that showed drastic reductions in

374 BC emissions during the lockdowns were those that suffered from the pandemic dramatically,

375 with many human losses, strict social distancing rules and consequently less transport.

376 Specifically, comparing with the previous five years, the 2020 emissions of BC during the

377 lockdowns dropped by 20% in Italy (3.4 to 2.7 kt), 40% in Germany (3.3 to 2.0 kt), 34% in

378 Spain (4.7 to 3.1 kt), 22% in France (3.5 to 2.7 kt) and remained the same or were slightly

379 enhanced in Poland (~9.2 kt), and Scandinavia (~1.2 kt). Overall, BC emissions during the 2020

380 lockdowns in Western Europe declined by 32% (8.8 to 6.0 kt), in Southern Europe by 42% (17

381 to 9.9 kt) and in Northern Europe by 29% (5.4 to 3.8 kt) as compared with the 2015–2019

382 period. BC emissions in Eastern Europe were slightly increased during the 2020 lockdown as

383 compared to the same period in the last five years (28 to 31 kt). The hot-spot emissions in

384 Eastern Europe coincide with the presence of active fires as revealed from MODIS (Figure 5a).

385  Note that these numbers correspond to BC emissions during the COVID-19 lockdown period
386  only (mid-March – April 2020).

387      Some localised areas of increased BC emissions exist in Southern France, Belgium,
388  Northern Germany and Eastern Europe (Figure 5), which are observed relative to almost every
389  year since 2015 (Supplementary Figure 1). While some hotspots in France cannot be easily
390  explained, increased emissions in Eastern European countries are likely due to increased
391  residential combustion, as people had to stay home during the lockdown. The combination of
392  the financial consequences of the COVID-19 lockdown with the relatively low GDP per capita
393  in these countries and the fact that from mid-March to end of April 2020 surface temperatures
394  in these countries were significantly lower than in previous years is suggestive of increased
395  emissions due to residential combustion. This source is most important in Eastern Europe
396  (Klimont et al., 2017). Although residential combustion can be performed for heating or
397  cooking needs in poorer countries, it is also believed to provide a more natural type of warmth
398  and a comfortable and relaxing environment. Hence, it should not be assumed as an emission
399  source in countries with lower GDPs only, especially as people spent more time at home.
400  Moreover, the prevailing average temperatures over Europe during the lockdown were below
401  15°C (Supplementary Figure 2), a temperature used as a basis temperature below which
402  residential combustion increases (Quayle and Diaz, 1980; Stohl et al., 2013).

### 3.3   Uncertainty and validation of the posterior emissions

404      One of the basic problems when dealing with inverse modelling is that changing model,
405  observational, or prior uncertainties can have drastic impacts on posterior emissions. We
406  addressed this issue by finding the optimal parameters, in order to have a reduced $\chi^2$ statistic
407  around unity (see section 2.3). However, there are two other sources of uncertainty that,
408  although not linked with the inversion algorithm, could affect posterior emissions drastically.
409  The first is the use of different prior emissions; to estimate this type of uncertainty, we
410  performed five inversions for January to April 2020 using each of the prior emission datasets
411  (ECLIPSEv6 and v5, EDGAR_HTAPv2.2, ACCMIPv5 and PKU). The uncertainty was
412  calculated as the gridded standard deviation of the posterior emissions resulting from the five
413  inversions. The second type of uncertainty concerns measurement of BC, which is defined as a
414  function of five properties (Petzold et al., 2013). However, as of today, no single instrument
415  exists that could measure all of these properties at the same time. Hence, BC is not a single
416  particle conistuent, rather an operational definition depending on the measurement technique
417  (Petzold et al., 2013). Here we use light absorption coefficients (Petzold et al., 2013) converted

to equivalent BC (eBC) using the mass absorption cross section (MAC). The MAC is instrument specific and wavelength dependent. The site-specific MAC values used to convert the filter-based light absorption to eBC can be seen in Table 1. It has been reported that MAC values vary from $2 - 3$ m$^2$ g$^{-1}$ up to 20 m$^2$ g$^{-1}$ (Bond and Bergstrom, 2006). To estimate the uncertainty of the posterior fluxes associated with the variable MAC, we performed a sensitivity study for January to April 2020 using MAC values of 5, 10 and 20 m$^2$ g$^{-1}$ in all stations, as well as variable MAC values for each station (Table 1). Since these values are lognormally distributed, the uncertainty is calculated as the geometric standard deviation. The impact of other sources of uncertainty, such as those referring to scavenging coefficients, particle size and density that are used in the model have been studied before and are significantly smaller than the sources of uncertainty that are considered here (Evangeliou et al., 2018; Grythe et al., 2017).

The posterior emissions are less sensitive to the use of different MACs than the use of different prior inventories (Figure 6). The relative uncertainty due to different use of MAC values was up to 20–30% in most of Europe and increases dramatically (~100%) far from the observations. The emission uncertainty of BC from the use of different priors was estimated to be up to 40% in Europe and shows very similar characteristics (same hot-spot regions and larger values where measurements lack). Overall, the combined uncertainty of BC emissions was ~60% in Europe.

Validation of top-down emissions obtained by inversion algorithms can be proper only if measurements that were not included in the inversion are to be used (independent observations). For this reason, we left out of the inversion observations from two stations (DE0054K and DE0066R, Table 1). Due to the higher measurement station density in Central Europe, we randomly selected two German stations, rather than from a country that is adjacent to regions that lack observations.

The prior, optimized and measured concentrations are shown in Figure 7 together with MERRA-2 surface BC concentrations at the same stations. The average footprint emission sensitivities are also given for the period of the lockdown. At station DE0054K, prior emissions represent observations very well until the beginning of the lockdown and then fail (Figure 7). On the other hand, the posterior emissions represent the variant concentrations during the lockdown effectively and also manage to capture some concentration peaks, which is reflected by lower $nRMSE$. Backward modelling showed that the enhanced concentrations originate from Northern Germany and the Netherlands, where posterior emissions were increased compared with the prior ones (Figure 4). A similar pattern was seen at station DE0066K,

451 although this station showed concentrations up to 4 mg m$^{-3}$ (Figure 7). Again, the optimized
452 emissions managed to represent the peaks at the end of January 2020 and at the beginning of
453 the lockdown, which is again reflected by a half *nRMSE* values and *MFB* close to zero as
454 compared to the priors. The larger concentrations during the lockdown result from increased
455 emissions over Eastern Germany, Poland and the Netherlands, as well as in oil industries in the
456 North Sea (Figure 4b). In all these regions the footprint emissions sensitivities corresponding
457 to the two independent stations were the highest.

## 4  Discussion

459 The improved air quality that Europe during the lockdown was also evident from the
460 assimilated MERRA-2 satellite-based BC data. The latter are plotted in Supplementary Figure
461 3 (left axis) for 2015–2020, together with the posterior emissions calculated in the present study
462 (right axis). For instance, weekly average concentrations of BC over Europe in MERRA-2
463 (Supplementary Figure 3, bottom). Many of the ACTRIS stations reported increased light
464 absorption in the beginning of the lockdown (e.g., Figure 7); MERRA-2 data show the same
465 patterns in France, Italy, UK and in Spain, and in all of Europe, in general. This can be explained
466 by residential combustion considering that the surface temperature during the lockdown was
467 lower than in previous years (Figure 5). The latter was confirmed by MERRA-2 reanalysis
468 Ångström Exponent (AE) parameter at 470–870 nm, which shows higher values over Central
469 and Eastern Europe during the lockdown in 2020 than in the same period of the previous years
470 (Figure 8a,b). Larger AE values confirm the presence of wood burning aerosols (Eck et al.,
471 1999). The fact that during the COVID-19 lockdown, residential combustion was a significant
472 aerosol source in Europe, as compared to the previous years, was also confirmed by real-time
473 observations of absorption AE from the AERONET data in five selected stations over Europe
474 (Figure 8c). Measured absorption AE was higher during mid-March to April 2020 than in the
475 same period of the last five years.

476 Emissions of BC calculated with Bayesian inversion for the lockdown period dropped
477 substantially in most of the countries that suffered from further spread of the virus and,
478 accordingly, from strict lockdown measures, as compared to the respective emissions before
479 the lockdowns (Supplementary Figure 3). Specifically, the decrease in France was as high as
480 42%, 8% in Italy, 21% in Germany, 11% in Spain and 13% in the UK. Emissions also declined
481 in Scandinavia by 5%, although Sweden did not enforce a lockdown. Overall, a reduction in
482 BC emissions of about 11% can be concluded for Europe as a whole due to the lockdown.

483    Stronger decreases in Eastern Europe were likely partly compensated by increased residential
484    combustion in resulting from the prevailing low temperatures.

485    We report a 23 kt decrease in BC emissions in Europe during the lockdown that partially
486    resulted from the COVID-19 outbreak, as compared to the same period in all previous years
487    since 2015, based on particle light absorption measurements. We highlight these changes in BC
488    emissions partially as a result of COVID-19 restrictions by plotting the temporal variability of
489    the BC emissions in the 5 previous years (2015 – 2019) for France, Italy, Germany, Spain,
490    Scandinavia and Europe (Figure 9). We record decreases in BC emissions in France, Italy,
491    Germany and Scandinavia in mid-March to April 2020, opposite to what was estimated for all
492    years between 2015 and 2019, which is obviously due to COVID-19. The UK and Spain showed
493    a similar decrease in mid-March to April 2020 emissions as in all previous years (2015–2019).
494    However, the estimated posterior BC emissions during the 2020 lockdowns were significantly
495    lower than those of the same period in any of the previous years. Overall, emissions declined
496    by 20% in Italy, 40% in Germany, 34% in Spain, 22% in France and remained the same and
497    slightly enhanced in Scandinavia or Poland as compared to those of the last five years.

## 5 Conclusions

499    The impact of the COVID-19 lockdowns over Europe on the BC emissions, in response
500    to the pandemic was assessed in the present manuscript. Particle light absorption measurements
501    from 17 ACTRIS stations all around Europe were rapidly gathered and cleaned to produce a
502    high-quality product. The latter was used in a well-established Bayesian inversion framework
503    and BC emissions were optimised over Europe to better capture the observations. However,
504    one should be careful not to overinterpret the emission changes at regional scales, due to the
505    poor station data density used and the high resolution timesteps of the inversions (weekly
506    posterior emissions). We calculate that the optimised (posterior) BC emissions declined from
507    63 to 40 kt (23%) during the lockdowns over Europe, as compared to the same period in the
508    previous five years (2015–2019). The largest reductions were calculated for countries that
509    suffered from the pandemic dramatically, such as Italy (3.4 to 2.7 kt), Germany (3.3 to 2.0 kt),
510    Spain (4.7 to 3.1 kt), France (3.5 to 2.7 kt). BC emissions in Western Europe during the 2020
511    lockdowns were decreased from 8.8 to 6.0 kt (32%), in Southern Europe from 17 to 9.9 kt
512    (42%) and in Northern Europe from 5.4 to 3.8 kt (29%) as compared to the same period in the
513    last five years. BC emissions were slightly enhanced in Eastern Europe (from 28 to 31 kt) and
514    remained unchanged in Scandinavia during the lockdown, due to increased residential

515 combustion, as people had to stay home and temperatures at that time were the lowest of the
516 last five years. The presence of wood burning aerosols during the lockdowns was confirmed by
517 large MERRA-2 AE, as well as from absorption AE measurements from AERONET that were
518 higher in the lockdowns than in the same period of the last five years. The impact of the
519 European lockdowns on BC emissions was also confirmed by a 11% decrease of the posterior
520 emissions over Europe during the lockdowns, as compared to the period before, opposite to
521 what was calculated in the previous years, which is obviously due to COVID-19. This decrease
522 was more pronounced in France (42%), Italy (8%), Germany (21%), Spain (11%), UK (13%)
523 and in Scandinavian countries (5%). The full impact of the disastrous pandemic will likely take
524 years to assess. Nevertheless, with COVID-19 cases once again increasing in many countries,
525 the information presented here are essential to understand the full health and climate impacts
526 of lockdown measures.

527 *Data availability.* All measurement data and model outputs used for the present publication are
528 open and can be downloaded from https://doi.org/10.21336/gen.b5vj-sn33 or upon request to
529 the corresponding author. All prior emission datasets are also available for download. ECLIPSE
530 emissions can be obtained from
531 http://www.iiasa.ac.at/web/home/research/researchPrograms/air/Global_emissions.html,
532 EDGAR version HTAP_V2.2 from http://edgar.jrc.ec.europa.eu/methodology.php#, ACCMIP
533 version 5 from http://accent.aero.jussieu.fr/ACCMIP_metadata.php) and PKU from
534 http://inventory.pku.edu.cn. FLEXPART is open in public and can be downloaded from
535 https://www.flexpart.eu, so as FLEXINVERT+ from https://flexinvert.nilu.no. MERRA-2 re-
536 analysis data can be obtained from https://disc.gsfc.nasa.gov, so as AERONET measurements
537 from https://aeronet.gsfc.nasa.gov.

# References

560 Ackerman, a. S.: Reduction of Tropical Cloudiness by Soot, Science (80-. )., 288(5468),
561 1042–1047, doi:10.1126/science.288.5468.1042, 2000.
562 Adams, M. D.: Air pollution in Ontario, Canada during the COVID-19 State of Emergency,
563 Sci. Total Environ., 742, 140516, doi:10.1016/j.scitotenv.2020.140516, 2020.
564 Bauwens, M., Compernolle, S., Stavrakou, T., Müller, J. F., van Gent, J., Eskes, H., Levelt, P.
565 F., van der A, R., Veefkind, J. P., Vlietinck, J., Yu, H. and Zehner, C.: Impact of Coronavirus
566 Outbreak on NO2 Pollution Assessed Using TROPOMI and OMI Observations, Geophys.
567 Res. Lett., 47(11), 1–9, doi:10.1029/2020GL087978, 2020.
568 Bergamaschi, P., Krol, M., Meirink, J. F., Dentener, F., Segers, A., Van Aardenne, J., Monni,
569 S., Vermeulen, A. T., Schmidt, M., Ramonet, M., Yver, C., Meinhardt, F., Nisbet, E. G.,
570 Fisher, R. E., O'Doherty, S. and Dlugokencky, E. J.: Inverse modeling of European CH4
571 emissions 2001-2006, J. Geophys. Res. Atmos., 115(22), 1–18, doi:10.1029/2010JD014180,
572 2010.
573 Berman, J. D. and Ebisu, K.: Changes in U.S. air pollution during the COVID-19 pandemic,
574 Sci. Total Environ., 739, 139864, doi:10.1016/j.scitotenv.2020.139864, 2020.
575 Bond, T. C. and Bergstrom, R. W.: Light Absorption by Carbonaceous Particles: An
576 Investigative Review, Aerosol Sci. Technol., 40(1), 27–67, doi:10.1080/02786820500421521,
577 2006.
578 Bond, T. C., Doherty, S. J., Fahey, D. W., Forster, P. M., Berntsen, T., Deangelo, B. J.,
579 Flanner, M. G., Ghan, S., Kärcher, B., Koch, D., Kinne, S., Kondo, Y., Quinn, P. K., Sarofim,
580 M. C., Schultz, M. G., Schulz, M., Venkataraman, C., Zhang, H., Zhang, S., Bellouin, N.,
581 Guttikunda, S. K., Hopke, P. K., Jacobson, M. Z., Kaiser, J. W., Klimont, Z., Lohmann, U.,
582 Schwarz, J. P., Shindell, D., Storelvmo, T., Warren, S. G. and Zender, C. S.: Bounding the
583 role of black carbon in the climate system: A scientific assessment, J. Geophys. Res. Atmos.,
584 118(11), 5380–5552, doi:10.1002/jgrd.50171, 2013.
585 Buchard, V., Randles, C. A., da Silva, A. M., Darmenov, A., Colarco, P. R., Govindaraju, R.,
586 Ferrare, R., Hair, J., Beyersdorf, A. J., Ziemba, L. D. and Yu, H.: The MERRA-2 aerosol
587 reanalysis, 1980 onward. Part II: Evaluation and case studies, J. Clim., 30(17), 6851–6872,
588 doi:10.1175/JCLI-D-16-0613.1, 2017.

589    Cassiani, M., Stohl, A. and Brioude, J.: Lagrangian Stochastic Modelling of Dispersion in the
590    Convective Boundary Layer with Skewed Turbulence Conditions and a Vertical Density
591    Gradient: Formulation and Implementation in the FLEXPART Model, Boundary-Layer
592    Meteorol., 154(3), 367–390, doi:10.1007/s10546-014-9976-5, 2014.

593    Clarke, A. D. and Noone, K. J.: Soot in the arctic snowpack: a cause for perturbations in
594    radiative transfer, Atmos. Environ., 41(SUPPL.), 64–72, doi:10.1016/0004-6981(85)90113-1,
595    1985.

596    Conticini, E., Frediani, B. and Caro, D.: Can atmospheric pollution be considered a co-factor
597    in extremely high level of SARS-CoV-2 lethality in Northern Italy?, Environ. Pollut., 261,
598    114465, doi:10.1016/j.envpol.2020.114465, 2020.

599    Copernicus Climate Change Service (C3S): C3S ERA5-Land reanalysis . Copernicus Climate
600    Change Service, [online] Available from: https://cds.climate.copernicus.eu/cdsapp#!/home
601    (Accessed 31 August 2020), 2020.

602    Dantas, G., Siciliano, B., França, B. B., da Silva, C. M. and Arbilla, G.: The impact of
603    COVID-19 partial lockdown on the air quality of the city of Rio de Janeiro, Brazil, Sci. Total
604    Environ., 729, doi:10.1016/j.scitotenv.2020.139085, 2020.

605    Diffenbaugh, N. S., Field, C. B., Appel, E. A., Azevedo, I. L., Baldocchi, D. D., Burke, M.,
606    Burney, J. A., Ciais, P., Davis, S. J., Fiore, A. M., Fletcher, S. M., Hertel, T. W., Horton, D.
607    E., Hsiang, S. M., Jackson, R. B., Jin, X., Levi, M., Lobell, D. B., McKinley, G. A., Moore, F.
608    C., Montgomery, A., Nadeau, K. C., Pataki, D. E., Randerson, J. T., Reichstein, M., Schnell,
609    J. L., Seneviratne, S. I., Singh, D., Steiner, A. L. and Wong-Parodi, G.: The COVID-19
610    lockdowns: a window into the Earth System, Nat. Rev. Earth Environ., 1–12,
611    doi:10.1038/s43017-020-0079-1, 2020.

612    Dutheil, F., Baker, J. S. and Navel, V.: COVID-19 as a factor influencing air pollution?,
613    Environ. Pollut., 263, 2019–2021, doi:10.1016/j.envpol.2020.114466, 2020.

614    Eck, T. F., Holben, B. N., Reid, J. S., Smirnov, A., Neill, N. T. O., Slutsker, I. and Kinne, S.:
615    Wavelength dependence of the optical depth of biomass burning, urban, and desert dust
616    aerosols, J. Geophys. Res., 104(D24), 31333–31349, 1999.

617    Evangeliou, N., Thompson, R. L., Eckhardt, S. and Stohl, A.: Top-down estimates of black
618    carbon emissions at high latitudes using an atmospheric transport model and a Bayesian
619    inversion framework, Atmos. Chem. Phys., 18(20), doi:10.5194/acp-18-15307-2018, 2018.

620    Forster, C., Stohl, A. and Seibert, P.: Parameterization of convective transport in a Lagrangian
621    particle dispersion model and its evaluation, J. Appl. Meteorol. Climatol., 46(4), 403–422,
622    doi:10.1175/JAM2470.1, 2007.

623    Giglio, L., Descloitres, J., Justice, C. O. and Kaufman, Y. J.: An enhanced contextual fire
624    detection algorithm for MODIS, Remote Sens. Environ., 87(2–3), 273–282,
625    doi:10.1016/S0034-4257(03)00184-6, 2003.

626    Giglio, L., Randerson, J. T. and van der Werf, G. R.: Analysis of daily, monthly, and annual
627    burned area using the fourth-generation global fire emissions database (GFED4), J. Geophys.
628    Res. Biogeosciences, 118, 317–328, doi:10.1002/jgrg.20042, 2013, 2013.

629    Grythe, H., Kristiansen, N. I., Groot Zwaaftink, C. D., Eckhardt, S., Ström, J., Tunved, P.,
630    Krejci, R. and Stohl, A.: A new aerosol wet removal scheme for the Lagrangian particle
631    model FLEXPARTv10, Geosci. Model Dev., 10, 1447–1466, doi:10.5194/gmd-10-1447-
632    2017, 2017.

633    Gueymard, C. A. and Yang, D.: Worldwide validation of CAMS and MERRA-2 reanalysis
634    aerosol optical depth products using 15 years of AERONET observations, Atmos. Environ.,
635    225(November 2019), 117216, doi:10.1016/j.atmosenv.2019.117216, 2020.

636    He, G., Pan, Y. and Tanaka, T.: The short-term impacts of COVID-19 lockdown on urban air
637    pollution in China, Nat. Sustain., doi:10.1038/s41893-020-0581-y, 2020.

638    Hegg, D. A., Warren, S. G., Grenfell, T. C., Doherty, S. J., Larson, T. V. and Clarke, A. D.:

Source attribution of black carbon in arctic snow, Environ. Sci. Technol., 43(11), 4016–4021, doi:10.1021/es803623f, 2009.

Holben, B. N., Eck, T. F., Slutsker, I., Tanré, D., Buis, J. P., Setzer, A., Vermote, E., Reagan, J. A., Kaufman, Y. J., Nakajima, T., Lavenu, F., Jankowiak, I. and Smirnov, A.: AERONET—A Federated Instrument Network and Data Archive for Aerosol Characterization, Remote Sens. Environ., 66(1), 1–16, doi:10.1016/S0034-4257(98)00031-5, 1998.

Huang, C., Wang, Y., Li, X., Ren, L., Zhao, J., Hu, Y., Zhang, L., Fan, G., Xu, J., Gu, X., Cheng, Z., Yu, T., Xia, J., Wei, Y., Wu, W., Xie, X., Yin, W., Li, H., Liu, M., Xiao, Y., Gao, H., Guo, L., Xie, J., Wang, G., Jiang, R., Gao, Z., Jin, Q., Wang, J. and Cao, B.: Clinical features of patients infected with 2019 novel coronavirus in Wuhan, China, Lancet, 395(10223), 497–506, doi:10.1016/S0140-6736(20)30183-5, 2020.

Janssens-Maenhout, G., Crippa, M., Guizzardi, D., Dentener, F., Muntean, M., Pouliot, G., Keating, T., Zhang, Q., Kurokawa, J., Wankmüller, R., Denier Van Der Gon, H., Kuenen, J. J. P., Klimont, Z., Frost, G., Darras, S., Koffi, B. and Li, M.: HTAP-v2.2: A mosaic of regional and global emission grid maps for 2008 and 2010 to study hemispheric transport of air pollution, Atmos. Chem. Phys., 15(19), 11411–11432, doi:10.5194/acp-15-11411-2015, 2015.

Jinhuan, Q. and Liquan, Y.: Variation characteristics of atmospheric aerosol optical depths and visibility in North China during 1980 } 1994, Atmos. Environ., 34, 603–609, 2000.

John Hopkins University of Medicine: Coronavirus resource center, [online] Available from: https://coronavirus.jhu.edu/map.html (Accessed 10 August 2020), 2020.

Kaminski, T., Rayner, P. J., Heimann, M. and Enting, I. G.: On aggregation errors in atmospheric transport inversions, J. Geophys. Res. Atmos., 106(D5), 4703–4715, doi:10.1029/2000JD900581, 2001.

Kerimray, A., Baimatova, N., Ibragimova, O. P., Bukenov, B., Kenessov, B., Plotitsyn, P. and Karaca, F.: Assessing air quality changes in large cities during COVID-19 lockdowns: The impacts of traffic-free urban conditions in Almaty, Kazakhstan, Sci. Total Environ., 730, 139179, doi:10.1016/j.scitotenv.2020.139179, 2020.

Klimont, Z., Kupiainen, K., Heyes, C., Purohit, P., Cofala, J., Rafaj, P., Borken-Kleefeld, J. and Schöpp, W.: Global anthropogenic emissions of particulate matter including black carbon, Atmos. Chem. Phys., 17, 8681–8723, doi:10.5194/acp-17- 50 8681-2017, 2017.

Kummu, M., Taka, M. and Guillaume, J. H. A.: Data from: Gridded global datasets for Gross Domestic Product and Human Development Index over 1990-2015, v2, Dryad, Dataset, doi:https://doi.org/10.5061/dryad.dk1j0, 2020.

Lack, D. A. and Langridge, J. M.: On the attribution of black and brown carbon light absorption using the Ångström exponent, Atmos. Chem. Phys., 13(20), 10535–10543, doi:10.5194/acp-13-10535-2013, 2013.

Laj, P., Bigi, A., Rose, C., Andrews, E., Lund Myhre, C., Collaud Coen, M., Wiedensohler, A., Schultz, M., Ogren, J., Fiebig, M., Gliß, J., Mortier, A., Pandolfi, M., Petäjä, T., Kim, S.-W., Aas, W., Putaud, J.-P., Mayol-Bracero, O., Keywood, M., Labrador, L., Aalto, P., Ahlberg, E., Alados Arboledas, L., Alastuey, A., Andrade, M., Artíñano, B., Ausmeel, S., Arsov, T., Asmi, E., Backman, J., Baltensperger, U., Bastian, S., Bath, O., Beukes, J. P., Brem, B., Bukowiecki, N., Conil, S., Couret, C., Day, D., Dayantolis, W., Degorska, A., Dos Santos, S. M., Eleftheriadis, K., Fetfatzis, P., Favez, O., Flentje, H., Gini, M., Gregorič, A., Gysel-Beer, M., Hallar, G., Hand, J., Hoffer, A., Hueglin, C., Hooda, R., Hyvärinen, A., Kalapov, I., Kalivitis, N., Kasper-Giebl, A., Kim, J. E., Kouvarakis, G., Kranjc, I., Krejci, R., Kulmala, M., Labuschagne, C., Lee, H.-J., Lihavainen, H., Lin, N.-H., Löschau, G., Luoma, K., Marinoni, A., Meinhardt, F., Merkel, M., Metzger, J.-M., Mihalopoulos, N., Nguyen, N. A., Ondracek, J., Peréz, N., Perrone, M. R., Petit, J.-E., Picard, D., Pichon, J.-M., Pont, V., Prats, N., Prenni, A., Reisen, F., Romano, S., Sellegri, K., Sharma, S., Schauer, G., Sheridan,

689    P., Sherman, J. P., Schütze, M., Schwerin, A., Sohmer, R., Sorribas, M., Steinbacher, M.,
690    Sun, J., Titos, G., Tokzko, B., et al.: A global analysis of climate-relevant aerosol properties
691    retrieved from the network of GAW near-surface observatories, Atmos. Meas. Tech. Discuss.,
692    1–70, doi:10.5194/amt-2019-499, 2020.
693    Lamarque, J. F., Shindell, D. T., Josse, B., Young, P. J., Cionni, I., Eyring, V., Bergmann, D.,
694    Cameron-Smith, P., Collins, W. J., Doherty, R., Dalsoren, S., Faluvegi, G., Folberth, G.,
695    Ghan, S. J., Horowitz, L. W., Lee, Y. H., MacKenzie, I. A., Nagashima, T., Naik, V.,
696    Plummer, D., Righi, M., Rumbold, S. T., Schulz, M., Skeie, R. B., Stevenson, D. S., Strode,
697    S., Sudo, K., Szopa, S., Voulgarakis, A. and Zeng, G.: The atmospheric chemistry and climate
698    model intercomparison Project (ACCMIP): Overview and description of models, simulations
699    and climate diagnostics, Geosci. Model Dev., 6(1), 179–206, doi:10.5194/gmd-6-179-2013,
700    2013.
701    Le, T., Wang, Y., Liu, L., Yang, J., Yung, Y. L., Li, G. and Seinfeld, J. H.: Unexpected air
702    pollution with marked emission reductions during the COVID-19 outbreak in China, Science
703    (80-. )., (2), eabb7431, doi:10.1126/science.abb7431, 2020.
704    Lian, X., Huang, J., Huang, R., Liu, C., Wang, L. and Zhang, T.: Impact of city lockdown on
705    the air quality of COVID-19-hit of Wuhan city, Sci. Total Environ., 742, 140556,
706    doi:10.1016/j.scitotenv.2020.140556, 2020.
707    Long, C. M., Nascarella, M. A. and Valberg, P. A.: Carbon black vs. black carbon and other
708    airborne materials containing elemental carbon: Physical and chemical distinctions, Environ.
709    Pollut., 181, 271–286, doi:10.1016/j.envpol.2013.06.009, 2013.
710    Myhre, G., Samset, B. H., Schulz, M., Balkanski, Y., Bauer, S., Berntsen, T. K., Bian, H.,
711    Bellouin, N., Chin, M., Diehl, T., Easter, R. C., Feichter, J., Ghan, S. J., Hauglustaine, D.,
712    Iversen, T., Kinne, S., Kirkevåg, A., Lamarque, J. F., Lin, G., Liu, X., Lund, M. T., Luo, G.,
713    Ma, X., Van Noije, T., Penner, J. E., Rasch, P. J., Ruiz, A., Seland, Skeie, R. B., Stier, P.,
714    Takemura, T., Tsigaridis, K., Wang, P., Wang, Z., Xu, L., Yu, H., Yu, F., Yoon, J. H., Zhang,
715    K., Zhang, H. and Zhou, C.: Radiative forcing of the direct aerosol effect from AeroCom
716    Phase II simulations, Atmos. Chem. Phys., 13(4), 1853–1877, doi:10.5194/acp-13-1853-2013,
717    2013.
718    Otmani, A., Benchrif, A., Tahri, M., Bounakhla, M., Chakir, E. M., El Bouch, M. and
719    Krombi, M.: Impact of Covid-19 lockdown on PM10, SO2 and NO2 concentrations in Salé
720    City (Morocco), Sci. Total Environ., 735(2), 139541, doi:10.1016/j.scitotenv.2020.139541,
721    2020.
722    Petzold, A., Ogren, J. A., Fiebig, M., Laj, P., Li, S. M., Baltensperger, U., Holzer-Popp, T.,
723    Kinne, S., Pappalardo, G., Sugimoto, N., Wehrli, C., Wiedensohler, A. and Zhang, X. Y.:
724    Recommendations for reporting black carbon measurements, Atmos. Chem. Phys., 13(16),
725    8365–8379, doi:10.5194/acp-13-8365-2013, 2013.
726    Pisso, I., Sollum, E., Grythe, H., Kristiansen, N., Cassiani, M., Eckhardt, S., Arnold, D.,
727    Morton, D., Thompson, R. L., Groot Zwaaftink, C. D., Evangeliou, N., Sodemann, H.,
728    Haimberger, L., Henne, S., Brunner, D., Burkhart, J. F., Fouilloux, A., Brioude, J., Philipp,
729    A., Seibert, P. and Stohl, A.: The Lagrangian particle dispersion model FLEXPART version
730    10.4, Geosci. Model Dev., 12, 4955–4997, doi:10.5194/gmd-12-4955-2019, 2019.
731    Qin, W., Zhang, Y., Chen, J., Yu, Q., Cheng, S., Li, W., Liu, X. and Tian, H.: Variation,
732    sources and historical trend of black carbon in Beijing, China based on ground observation
733    and MERRA-2 reanalysis data, Environ. Pollut., 245(2), 853–863,
734    doi:10.1016/j.envpol.2018.11.063, 2019.
735    Quayle, R. G. and Diaz, H. F.: Heating degree day data applied to residential heating energy
736    consumption, J. Appl. Meteorol., 19, 241–246, 1980.
737    Le Quéré, C., Jackson, R. B., Jones, M. W., Smith, A. J. P., Abernethy, S., Andrew, R. M.,
738    De-Gol, A. J., Willis, D. R., Shan, Y., Canadell, J. G., Friedlingstein, P., Creutzig, F. and

739    Peters, G. P.: Temporary reduction in daily global CO2 emissions during the COVID-19
740    forced confinement, Nat. Clim. Chang., 10(7), 647–653, doi:10.1038/s41558-020-0797-x,
741    2020.
742    Randles, C. A., da Silva, A. M., Buchard, V., Colarco, P. R., Darmenov, A., Govindaraju, R.,
743    Smirnov, A., Holben, B., Ferrare, R., Hair, J., Shinozuka, Y. and Flynn, C. J.: The MERRA-2
744    aerosol reanalysis, 1980 onward. Part I: System description and data assimilation evaluation,
745    J. Clim., 30(17), 6823–6850, doi:10.1175/JCLI-D-16-0609.1, 2017.
746    Sicard, P., De Marco, A., Agathokleous, E., Feng, Z., Xu, X., Paoletti, E., Rodriguez, J. J. D.
747    and Calatayud, V.: Amplified ozone pollution in cities during the COVID-19 lockdown, Sci.
748    Total Environ., 735, doi:10.1016/j.scitotenv.2020.139542, 2020.
749    Sohrabi, C., Alsafi, Z., O'Neill, N., Khan, M., Kerwan, A., Al-Jabir, A., Iosifidis, C. and
750    Agha, R.: World Health Organization declares global emergency: A review of the 2019 novel
751    coronavirus (COVID-19), Int. J. Surg., 76(February), 71–76, doi:10.1016/j.ijsu.2020.02.034,
752    2020.
753    Stohl, A., Forster, C., Frank, A., Seibert, P. and Wotawa, G.: Technical note: The Lagrangian
754    particle dispersion model FLEXPART version 6.2, Atmos. Chem. Phys., 5(9), 2461–2474,
755    doi:10.5194/acp-5-2461-2005, 2005.
756    Stohl, A., Kim, J., Li, S., O'Doherty, S., Salameh, P. K., Saito, T., Vollmer, M. K., Wan, D.,
757    Yao, B., Yokouchi, Y. and Zhou, L. X.: Hydrochlorofluorocarbon and hydrofluorocarbon
758    emissions in East Asia determined by inverse modeling, Atmos. Chem. Phys. Discuss., 10(2),
759    2089–2129, doi:10.5194/acpd-10-2089-2010, 2010.
760    Stohl, A., Klimont, Z., Eckhardt, S., Kupiainen, K., Shevchenko, V. P., Kopeikin, V. M. and
761    Novigatsky, A. N.: Black carbon in the Arctic: The underestimated role of gas flaring and
762    residential combustion emissions, Atmos. Chem. Phys., 13(17), 8833–8855, doi:10.5194/acp-
763    13-8833-2013, 2013.
764    Sun, E., Xu, X., Che, H., Tang, Z., Gui, K., An, L., Lu, C. and Shi, G.: Variation in MERRA-
765    2 aerosol optical depth and absorption aerosol optical depth over China from 1980 to 2017, J.
766    Atmos. Solar-Terrestrial Phys., 186(January), 8–19, doi:10.1016/j.jastp.2019.01.019, 2019.
767    Tarantola, A.: Inverse Problem Theory and Methods for Model Parameter Estimation, Society
768    for Industrial and Applied Mathematics, Philadelphia, Pa., 2005.
769    Thacker, W. C.: Data assimilation with inequality constraints, Ocean Model., 16(3–4), 264–
770    276, doi:10.1016/j.ocemod.2006.11.001, 2007.
771    Thompson, R. L. and Stohl, A.: FLEXINVERT: An atmospheric Bayesian inversion
772    framework for determining surface fluxes of trace species using an optimized grid, Geosci.
773    Model Dev., 7(5), 2223–2242, doi:10.5194/gmd-7-2223-2014, 2014.
774    Thompson, R. L., Stohl, A., Zhou, L. X., Dlugokencky, E., Fukuyama, Y., Tohjima, Y., Kim,
775    S. Y., Lee, H., Nisbet, E. G., Fisher, R. E., Lowry, D., Weiss, R. F., Prinn, R. G., O'Doherty,
776    S., Young, D. and White, J. W. C.: Methane emissions in East Asia for 2000-2011 estimated
777    using an atmospheric Bayesian inversion, J. Geophys. Res. Atmos., 120(9), 4352–4369,
778    doi:10.1002/2014JD022394, 2015.
779    Wang, P., Wang, H., Wang, Y. Q., Zhang, X. Y., Gong, S. L., Xue, M., Zhou, C. H., Liu, H.
780    L., An, X. Q., Niu, T. and Cheng, Y. L.: Inverse modeling of black carbon emissions over
781    China using ensemble data assimilation, Atmos. Chem. Phys., 16(2), 989–1002,
782    doi:10.5194/acp-16-989-2016, 2016.
783    Wang, R., Tao, S., Balkanski, Y., Ciais, P., Boucher, O., Liu, J., Piao, S., Shen, H., Vuolo, M.
784    R., Valari, M., Chen, H., Chen, Y., Cozic, A., Huang, Y., Li, B., Li, W., Shen, G., Wang, B.
785    and Zhang, Y.: Exposure to ambient black carbon derived from a unique inventory and high-
786    resolution model., Proc. Natl. Acad. Sci. U. S. A., 111(7), 2459–63,
787    doi:10.1073/pnas.1318763111, 2014a.
788    Wang, R., Tao, S., Shen, H., Huang, Y., Chen, H., Balkanski, Y., Boucher, O., Ciais, P.,

789  Shen, G., Li, W., Zhang, Y., Chen, Y., Lin, N., Su, S., Li, B., Liu, J. and Liu, W.: Trend in
790  global black carbon emissions from 1960 to 2007, Environ. Sci. Technol., 48(12), 6780–6787,
791  doi:10.1021/es5021422, 2014b.
792  WHO: Report of the WHO-China Joint Mission on Coronavirus Disease 2019 (COVID-19),
793  WHO-China Jt. Mission Coronavirus Dis. 2019, 2019(February), 16–24 [online] Available
794  from: https://www.who.int/docs/default-source/coronaviruse/who-china-joint-mission-on-
795  covid-19-final-report.pdf, 2020.
796  Zanatta, M., Gysel, M., Bukowiecki, N., M??ller, T., Weingartner, E., Areskoug, H., Fiebig,
797  M., Yttri, K. E., Mihalopoulos, N., Kouvarakis, G., Beddows, D., Harrison, R. M., Cavalli, F.,
798  Putaud, J. P., Spindler, G., Wiedensohler, A., Alastuey, A., Pandolfi, M., Sellegri, K.,
799  Swietlicki, E., Jaffrezo, J. L., Baltensperger, U. and Laj, P.: A European aerosol
800  phenomenology-5: Climatology of black carbon optical properties at 9 regional background
801  sites across Europe, Atmos. Environ., 145, 346–364, doi:10.1016/j.atmosenv.2016.09.035,
802  2016.
803  Zheng, H., Kong, S., Chen, N., Yan, Y., Liu, D., Zhu, B., Xu, K., Cao, W., Ding, Q., Lan, B.,
804  Zhang, Z., Zheng, M., Fan, Z., Cheng, Y., Zheng, S., Yao, L., Bai, Y., Zhao, T. and Qi, S.:
805  Significant changes in the chemical compositions and sources of PM2.5 in Wuhan since the
806  city lockdown as COVID-19, Sci. Total Environ., 739, doi:10.1016/j.scitotenv.2020.140000,
807  2020.
808  Zotter, P., Herich, H., Gysel, M., El-Haddad, I., Zhang, Y., Mocnik, G., Hüglin, C.,
809  Baltensperger, U., Szidat, S. and Prévôt, A. S. H.: Evaluation of the absorption Ångström
810  exponents for traffic and wood burning in the Aethalometer-based source apportionment
811  using radiocarbon measurements of ambient aerosol, Atmos. Chem. Phys., 17(6), 4229–4249,
812  doi:10.5194/acp-17-4229-2017, 2017.
813
814

**TABLES & FIGURES**

816

**Table 1.** Observation sites from the ACTRIS platform used to perform the inversions (dependent observations) and to validate the posterior emissions (independent observations) (the altitude indicates the sampling height in meters above sea level). Multi-Angle Absorption Photometers (MAAP) were used at all sites, except El Arenosillo (ES0100R) where a Continuous Light Absorption Photometer (CLAP) was used, Birkenes (NO0002R), where a Particle Soot Absorption Photometer (PSAP) and Observatoire Perenne de l' Environnement (FR0022R) and Zeppelin (NO0042G) where Aethalometers (AW31) were used.

| Name | Latitude | Longitude | Altitude | Type | Wavelength (nm) | $MAC_{@637}$ $(m^2\ g^{-1})$ |
|---|---|---|---|---|---|---|
| Jungfraujoch (CH0001G) | 46.55 | 7.99 | 3578 | Dependent | 637 | 10 |
| Hohenpeissenberg (DE0043G) | 47.80 | 11.01 | 985 | Dependent | 660 | 9.65 |
| Melpitz (DE0044K) | 51.53 | 12.93 | 86 | Dependent | 670 | 8.78 |
| Zugspitze-Schneefernerhaus (DE0054R) | 47.42 | 10.98 | 2671 | Independent | 670 | 9.51 |
| Leipzig-Eisenbahnstrasse (DE0066K) | 51.35 | 12.41 | 120 | Independent | 670 | 9.51 |
| Izaña (ES0018G) | 28.41 | -16.50 | 2373 | Dependent | 670 | 9.51 |
| Granada (ES0020U) | 37.16 | -3.61 | 680 | Dependent | 670 | 9.51 |
| Montsec (ES0022R) | 42.05 | 0.73 | 1571 | Dependent | 670 | 9.51 |
| El Arenosillo (ES0100R) | 37.10 | -6.73 | 41 | Dependent | 652 | 13.64 |
| Montseny (ES1778R) | 41.77 | 2.35 | 700 | Dependent | 670 | 8.48 |
| Pallas (FI0096G) | 67.97 | 24.12 | 565 | Dependent | 637 | 10.00 |
| Observatoire Perenne de l' Environnement (FR0022R) | 48.56 | 5.51 | 392 | Dependent | 880 | 7.24 |
| Puy de Dôme (FR0030R) | 45.77 | 2.96 | 1465 | Dependent | 670 | 9.51 |
| Ispra (IT0004R) | 45.80 | 8.63 | 209 | Dependent | 880 | 6.96 |
| Mt Cimone (IT0009R) | 44.18 | 10.70 | 2165 | Dependent | 670 | 9.51 |
| Birkenes II (NO0002R) | 58.39 | 8.25 | 219 | Dependent | 660 | 7.59 |
| Zeppelin mountain (NO0042G) | 78.91 | 11.89 | 474 | Dependent | 880 | 7.24 |

824

**Table 2.** Statistical measures ($RMSE$, Pearson's $R^2$, $MFB$ and $nMAE$) for each of the prior and posterior concentrations against dependent observations (observations that were used in the inversion algorithm) for BC (eBC). Note that the inversion using ECLIPSEv6 prior emission dataset gave the best agreement with the observations and therefore the results of this inversion are presented here.

| | $nRMSE$ | Pearson's $R^2$ | MFB | nMAE |
|---|---|---|---|---|
| Prior ECLIPSEv6 | 0.102 | 0.30 | 0.52 | 997 |
| Prior ECLIPSEv5 | 0.098 | 0.18 | -0.04 | 996 |
| Prior EDGAR_HTAPv2.2 | 0.105 | 0.11 | 0.34 | 1017 |
| Prior ACCMIPv5 | 0.101 | 0.28 | 0.36 | 971 |
| Prior PKU | 0.101 | 0.21 | 0.25 | 983 |
| **Posterior ECLIPSEv6** | **0.073** | **0.60** | **0.03** | **714** |
| Posterior ECLIPSEv5 | 0.084 | 0.52 | 0.09 | 819 |
| Posterior EDGAR_HTAPv2.2 | 0.084 | 0.53 | 0.20 | 815 |
| Posterior ACCMIPv5 | 0.091 | 0.55 | 0.26 | 787 |
| Posterior PKU | 0.082 | 0.55 | 0.24 | 795 |
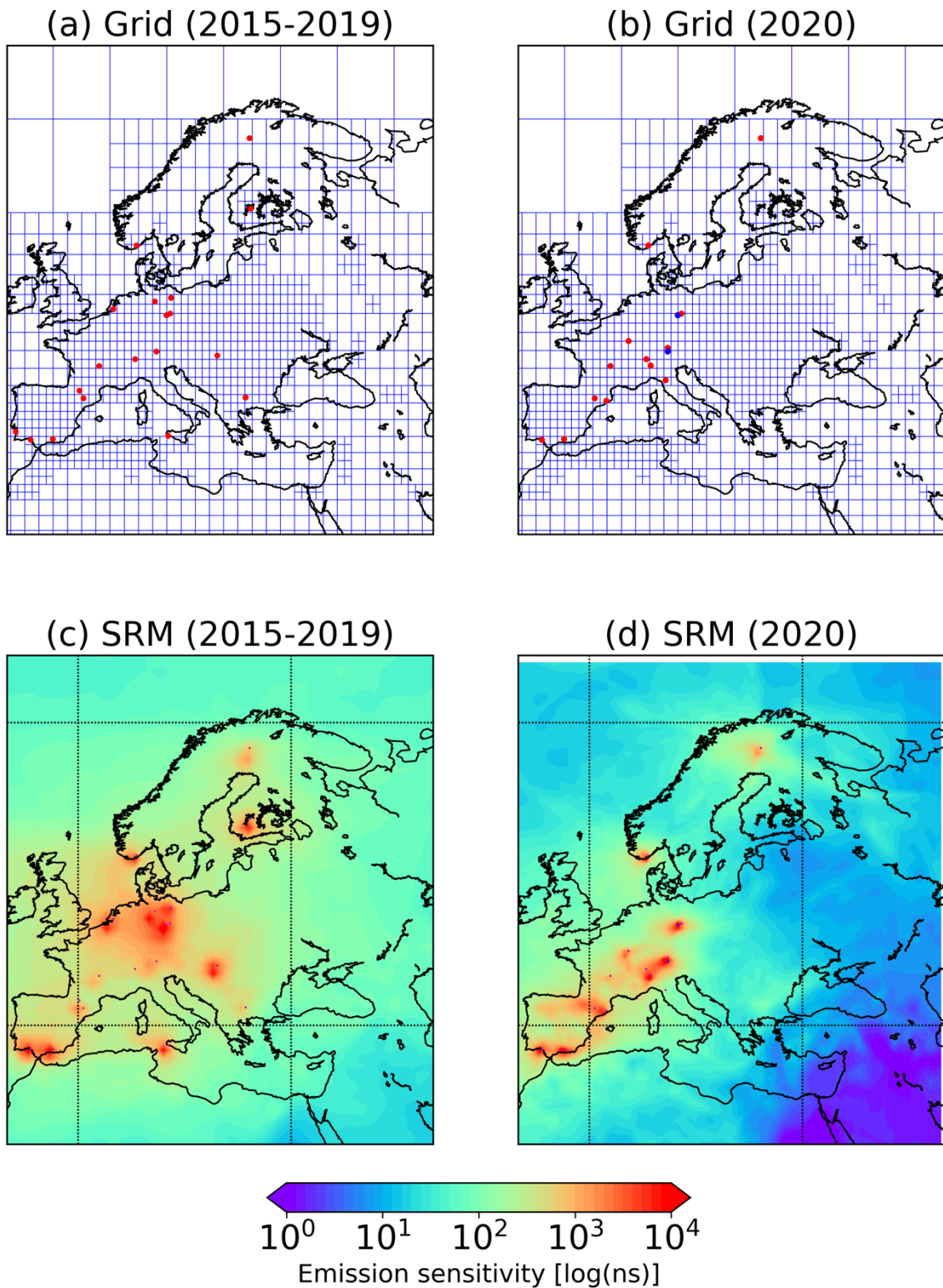
**Figure 1.** Aggregated inversion grid used for the (a) 2015–2019 and (b) 2020 inversions, respectively. The dependent measurements that were used in the inversion were taken from stations highlighted in red. The two independent stations that were used for the validation are shown in blue. (c, d) Footprint emission sensitivity (i.e. SRM) averaged over all observations and time steps for each of the inversions. Red points denote the location of each measurement site.
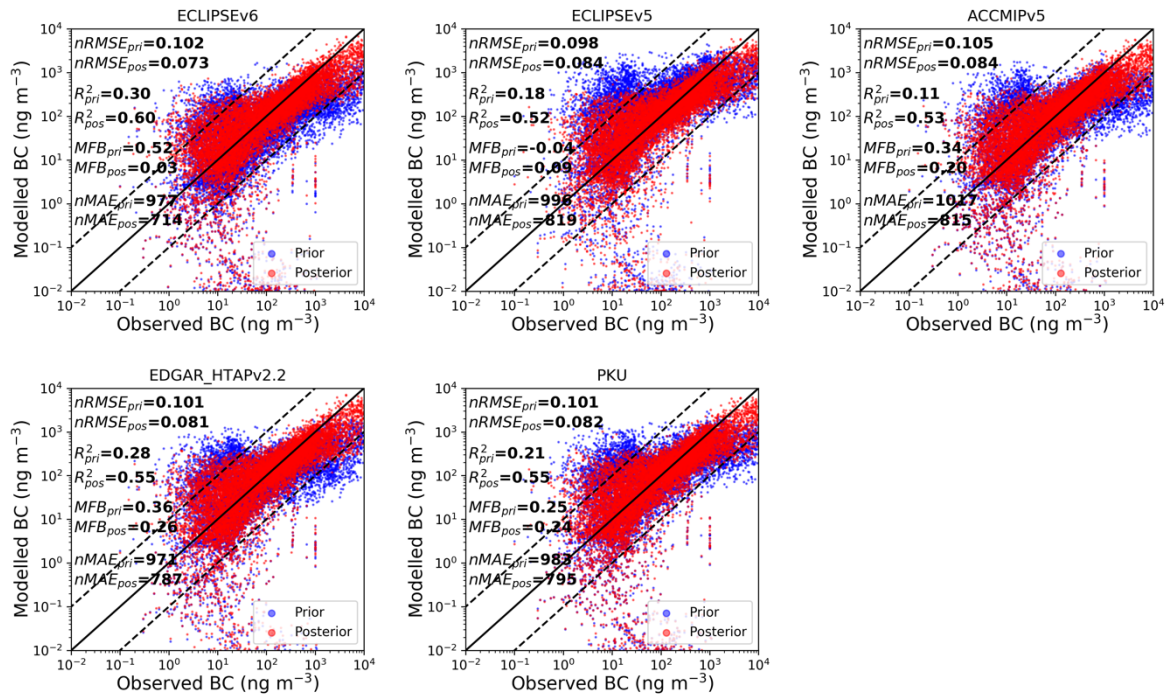
**Figure 2.** Scatter plots of prior and posterior concentrations against dependent observations (observations that were included in the inversion framework) from ACTRIS from January to April 2020. Four statistical measures (***nRMSE***, Pearson's $R^2$, ***MFB*** and ***nMAE***) were used to assess the performance of each inversion using five different prior emission inventories for BC (ECLIPSEv5, v6, ACCMIPv5, EDGAR_HTAPv2.2 and PKU).

**PRIOR EMISSIONS (JAN-APR 2020)**
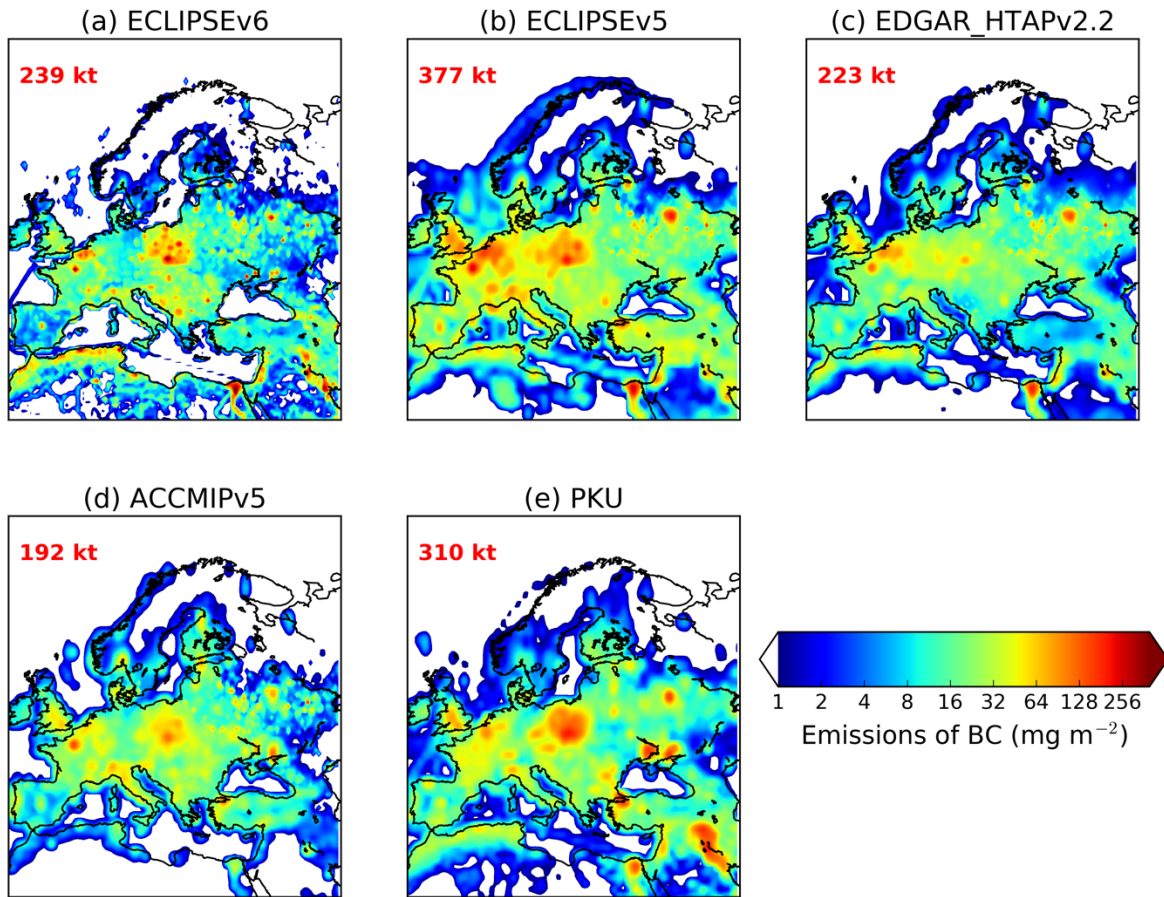


**Figure 3.** Prior emissions of black carbon (BC) used in the inversions. BC emissions from anthropogenic sources were adopted from ECLIPSE version 5 and 6 (Evaluating the CLimate and Air Quality ImPacts of ShortlivEd Pollutants) (Klimont et al., 2017), EDGAR (Emissions Database for Global Atmospheric Research) version HTAP_v2.2 (Janssens-Maenhout et al., 2015), ACCMIP (Emissions for Atmospheric Chemistry and Climate Model Intercomparison Project) version 5 (Lamarque et al., 2013) and PKU (Peking University) (Wang et al., 2014b). Biomass burning emissions of BC from Global Fire Emissions Database (GFED) version 4.1 (Giglio et al., 2013) were added in each of the aforementioned inventories.
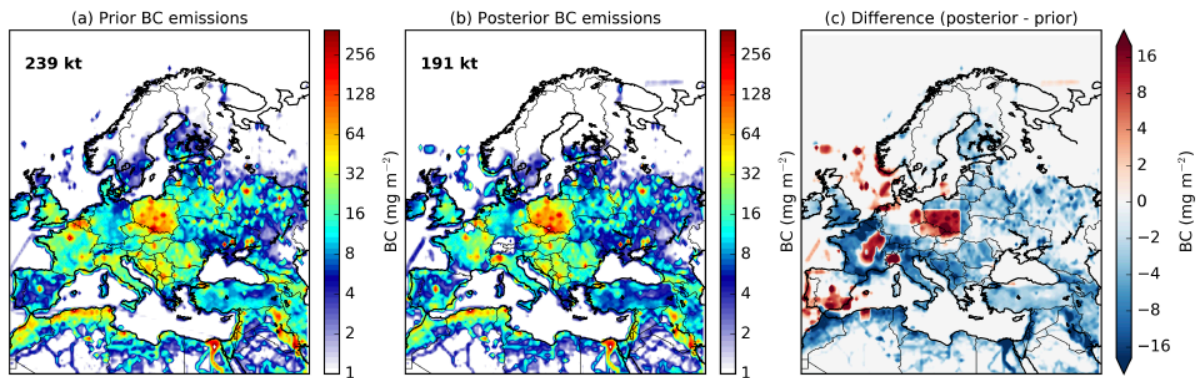
**Figure 4.** (a) Prior emissions of BC from ECLIPSEv6, (b) optimized (posterior) BC emissions after processing the ACTRIS data into the inversion algorithm, and (c) difference between posterior and prior emissions. All the results correspond to the inversion yielding the best results (**Table 2** and **Figure 2**).

**EMISSION ANOMALY, GDP, TEMPERATURE ANOMALY DURING THE LOCKDOWN PERIOD**
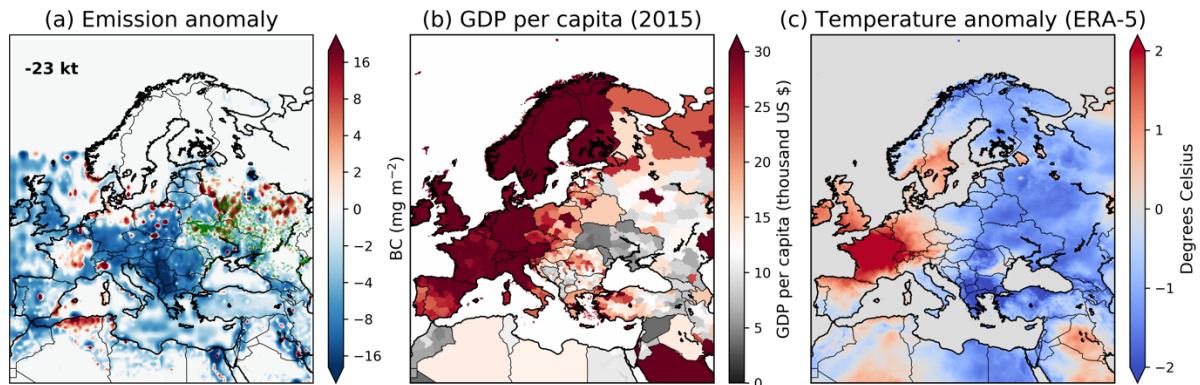


**Figure 5.** (a) Difference in posterior BC emissions during the lockdown (14 March to 30 April 2020) in Europe from the respective emissions during the same period in 2015 – 2019, (b) GDP from Kummu et al. (2020), and (c) temperature anomaly from ERA-5 (Copernicus Climate Change Service (C3S), 2020) for the same period as the emission anomaly. The base GDP value below which a low income can be assumed was set to 12 thousand US dollars. Active fires from MODIS are plotted together with emission anomaly (green dots).
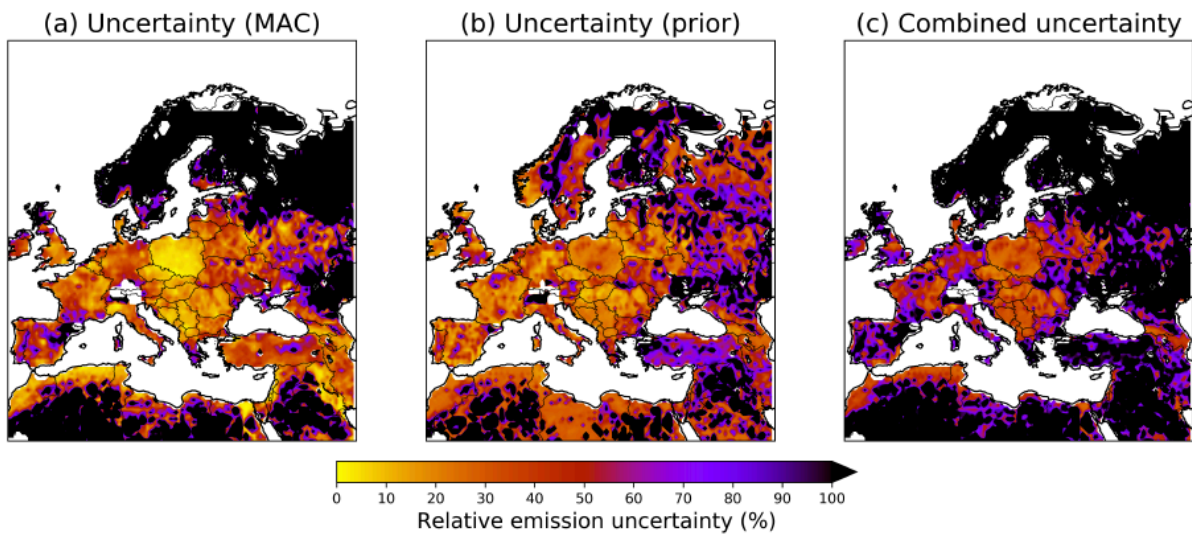
**Figure 6.** (a) Uncertainty of BC emissions due to the use of variable MAC values to convert from aerosol absorption to eBC concentrations that are used by the inversion algorithm. (b) Uncertainty due to the use of five different prior emissions inventories for BC. (c) Combined uncertainty.
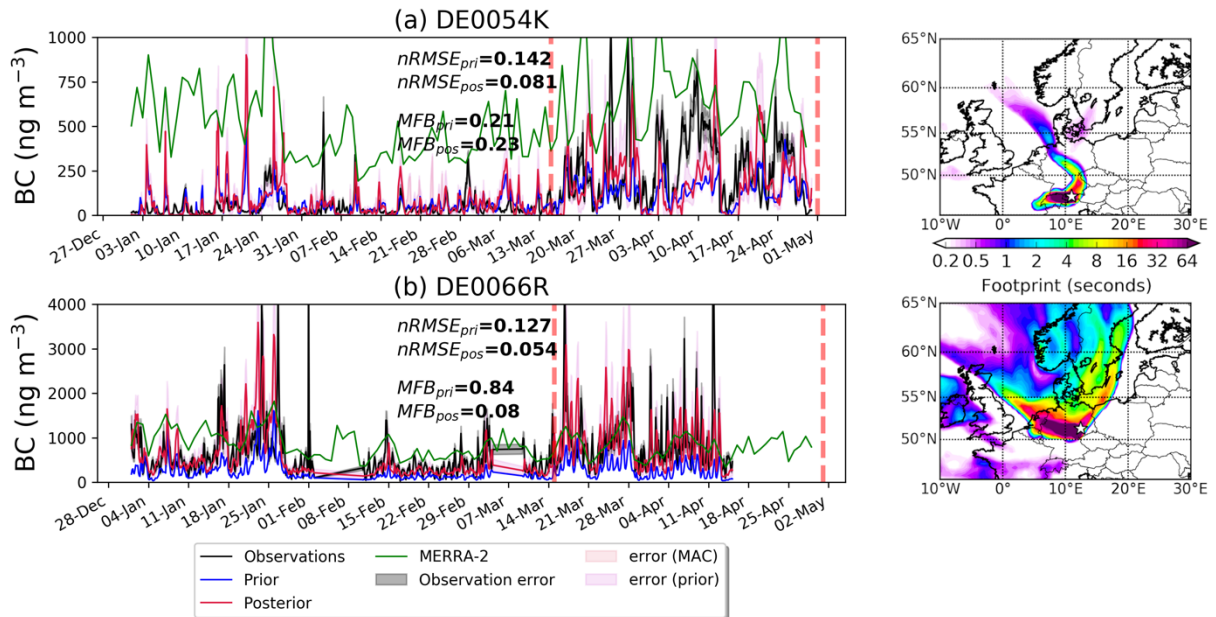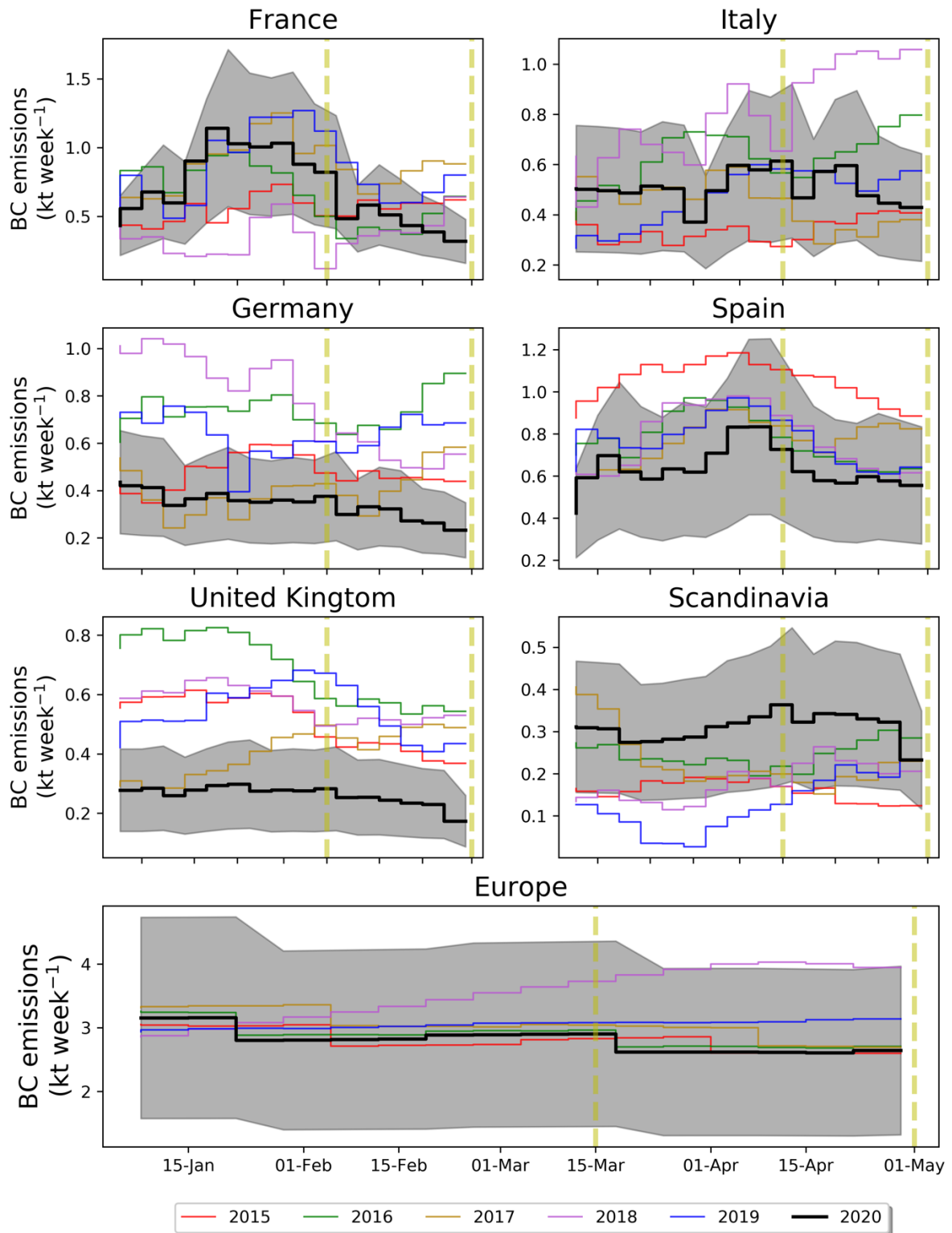
**Figure 7.** Prior and posterior BC concentrations at DE0054K and DE0066R stations that were not included in the inversion are compared with observations. The validation is done by calculating the ***nRMSEs*** and ***MFBs*** for the prior and posterior concentrations. The uncertainty of the observations is also given together with the posterior uncertainties in the concentrations calculated from the use of different MAC and prior emissions. For comparison, we plot the concentrations from MERRA-2 at the same two stations. The vertical dashed lines denote the period of the lockdown in most of Europe. On the right, the average footprint emission sensitivities are given at each independent station for the period of the lockdown.
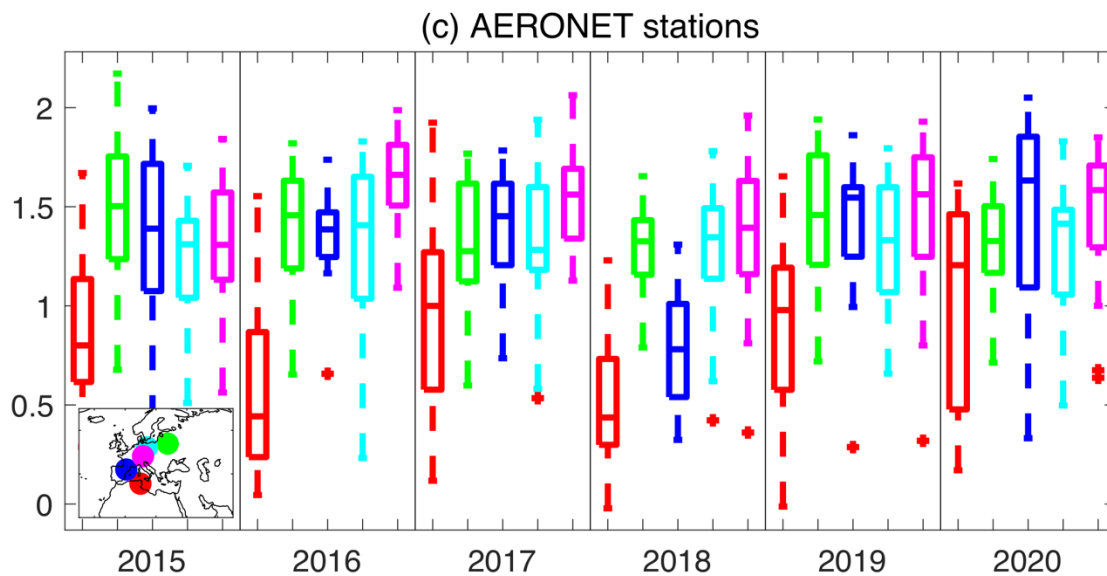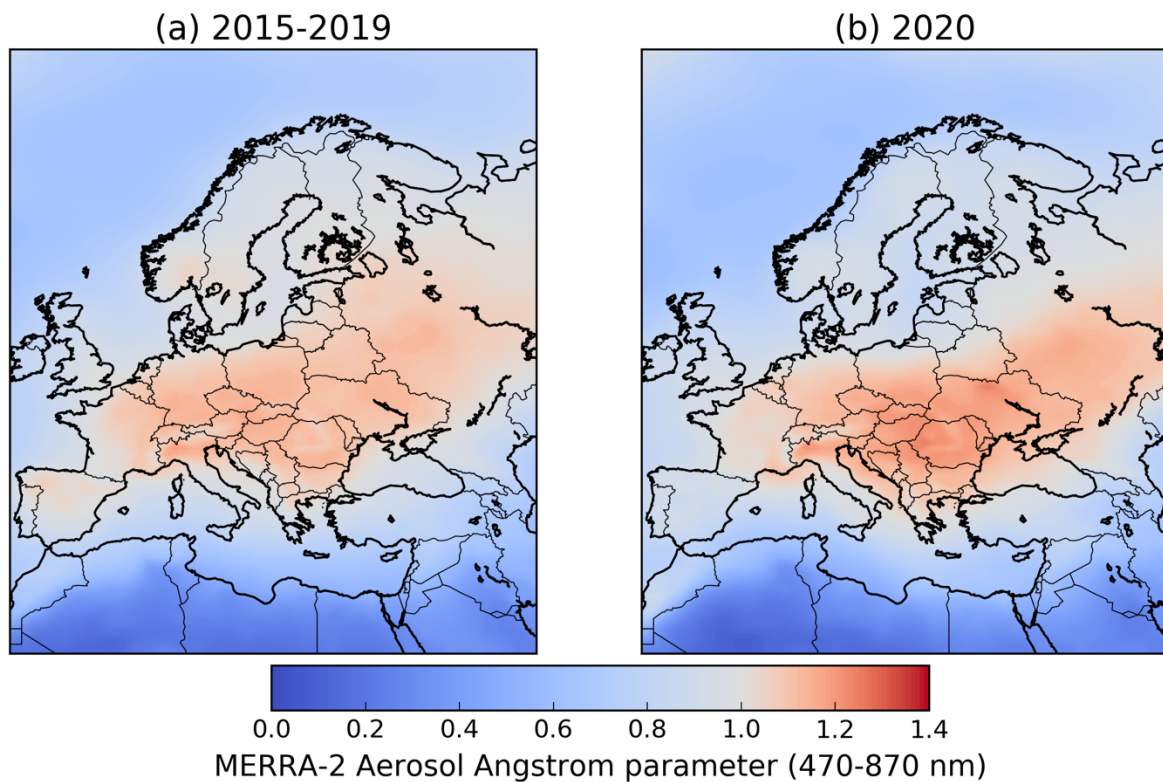
**Figure 8.** (a) Average total aerosol Ångström parameter (470-870 nm) over Europe (mid-March to April) in the five previous years (2015–2019) and (b) in 2020 (lockdown). (c) AERONET Absorption AE in Ben Salem (9.91°E, 35.55°N, in red), Minsk (27.60°E, 53.92°N, green), Montsec (0.73°E, 42.05°N, blue), MetObs Lindenberg (14.12°E, 52.21°N, magenta) and Munich University (11.57°E, 48.15°N) during mid-March to April in all years since 2015.

**Figure 9.** Posterior BC emissions in the most highly affected European countries (France, Italy, Germany, Spain and UK), Scandinavia and Europe from the COVID-19 pandemic (2020). Posterior BC emissions for every year since 2015 are also plotted in the same temporal resolution to show changes in BC emissions characteristics during the 2020 COVID-19 pandemic. The grey shaded area corresponds to the BC emission uncertainty, while the vertical yellow dashed lines correspond to the beginning and end of the 2020 lockdown.

**SUPPLEMENTARY FIGURE LEGENDS**

902

903 **Supplementary Figure 1. Comparison with BC emissions in previous years.**

904 Difference of optimised (posterior) BC emissions over Europe during the 2020 lockdown (14

905 March to 30 April) from respective BC emissions in previous years (same period) constrained

906 with the same inversion algorithm and the same settings. Active fires from MODIS are plotted

907 together with emission anomaly (green dots).

908 **Supplementary Figure 2. Surface temperature during the 2020 lockdown.**

909 Average surface temperature at 2 m over Europe during the COVID-19 lockdown (14 March

910 to 30 April) from ERA-5 (ECMWF)(Copernicus Climate Change Service (C3S), 2020). Note

911 that prevailing average temperatures over Europe during the lockdown were below 15°C. This

912 temperature has been used as the basis temperature, below which residential combustion has

913 been found to increase(Quayle and Diaz, 1980; Stohl et al., 2013).

914 **Supplementary Figure 3. Weekly posterior BC emissions against MERRA-2**

915 **concentrations.**

916 Average surface BC concentrations from MERRA-2 (left axis) since 2015 in the most highly

917 affected European countries (France, Italy, Germany, Spain and UK), Scandinavia and Europe

918 from the pandemic, in contrast to the calculated optimized BC emissions (right axis). The grey

919 shaded area corresponds to the BC emission uncertainty calculated as described in section 3.3.

920 The vertical yellow dashed lines correspond to the beginning and end of the COVID-19

921 lockdown (14 March to 30 April 2020).